

Printable Graphene Oxide Nanocomposites as Versatile Platforms for Immobilization of Functional Biomolecules

Alberto S. de León,* María de la Mata, Francisco J. Delgado, and Sergio I. Molina

A series of novel nanocomposites containing graphene oxide (GO) suitable for stereolithography is presented. Different loads of GO are tested, identifying that these materials can be printed with concentrations up to 2.5 wt% GO, presenting improved mechanical properties for concentrations below 1.0 wt% GO. In this range, the nanocomposites exhibit higher strength and toughness when compared to the pristine resin. Microscopic analyses of the material demonstrate that this can be correlated with the good compatibility of GO with the resin, which favors its homogeneous dispersion in the form of flexible nanoplates. After manufacturing, the availability of GO to participate in surface modification reactions with chitosan (CHI) and an alkaline phosphatase (ALP) is evaluated. CHI and ALP are well-known to act as biological cues in biorecognition processes, evidencing that these nanocomposites are suitable as platforms for selective immobilization of functional biomolecules.

AM can be used to create anatomically adapted scaffolds or wearable devices adapted for every patient according to their current necessities.^[8,9]

Stereolithography (SL) is an AM technique which allows the fabrication of objects in a layer-by-layer fashion using a photocurable liquid resin precursor that solidifies under the irradiation of a laser with a specific wavelength. Compared to other widespread AM techniques such as fused deposition modeling (FDM) or selective laser sintering (SLS), SL allows the manufacturing of more anatomically precise objects with higher resolution, down to few micrometers, at a competitive printing speed.^[10,11] Moreover, SL typically operates at room temperature, allowing to integrate temperature-sensitive bioactive molecules^[12,13] that would be degraded under standard processing conditions of FDM or SLS, usually above 200 °C.

1. Introduction


The development of 3D structures with controlled geometry, mechanical properties, and the ability of patterning biomolecules on surface are of great interest in different fields of biomedical research including protein immobilization,^[1] biosensors,^[2] implants,^[3] or tissue engineering.^[4] In the last decade, additive manufacturing (AM, also known as 3D printing) has contributed significantly to fabricate new materials that fulfill these requirements.^[5–7] Complex structures, which cannot be manufactured via classical techniques (e.g., compression molding), are created on demand by simply using a computer-assisted design (CAD) software. In combination with scanning techniques, including computed tomography or magnetic resonance imaging,

To enhance the mechanical and functional properties of the resins for SL, different fillers may be used as additives. Among other features, these additives must be well-dispersed avoiding segregation or sedimentation in the resin precursor. Too high additive concentration causes an excessive increase in the viscosity of the precursor, which limits its processability.^[14] Besides, additives generally absorb and scatter part of the intensity of the laser light decreasing the dose received by the photopolymer.^[15] These aspects cause the printing process to be defective. In this regard, nanomaterials, including graphene and graphene-derived materials, are presented as a promising alternative, since significant changes in the material properties are observed even for very low amounts.^[16,17]

Recently, the use of graphene oxide (GO) has been explored in the development of printable nanocomposites due to its high surface-to-volume ratio and good compatibility with the photocurable resins.^[18–22] GO is a 2D-like nanomaterial which has many polar, functional groups able to interact with the polymeric matrix via noncovalent interactions,^[23] permitting the fabrication of novel materials with enhanced mechanical properties. Printable nanocomposites with increased strength via SL have been reported by different authors following different strategies, including GO functionalization with a polymer or a compatible agent or post-processing at high temperature.^[20,23,24] In all these cases, the amount of GO remains below 1.0 wt%.

Moreover, different dispersion strategies, including melt compounding, solution-assisted mixing or high shear mixing have been tested to improve the compatibility and increase the amount of GO that can be added.^[18,25] For instance, Guo et al.^[26]

A. S. de León, M. de la Mata, F. J. Delgado, S. I. Molina
 Dpto. Ciencia de los Materiales
 I. M. y Q. I., IMEYMAT
 Facultad de Ciencias
 Universidad de Cádiz
 Campus Río San Pedro, s/n, Puerto Real, Cádiz 11510, Spain
 E-mail: alberto.sanzdeleon@uca.es

 The ORCID identification number(s) for the author(s) of this article can be found under <https://doi.org/10.1002/mame.202100784>

© 2022 The Authors. Macromolecular Materials and Engineering published by Wiley-VCH GmbH. This is an open access article under the terms of the Creative Commons Attribution License, which permits use, distribution and reproduction in any medium, provided the original work is properly cited.

DOI: 10.1002/mame.202100784

have recently proved that GO ultrasonication in presence of a dispersant agent allowed to increase the GO content up to 5 wt%, which led to significant changes in the electrical conductivity. These results are promising for the design of durable, biosensors or real-time monitorization of patient-adapted wearable devices.^[27] GO has also shown good biocompatibility with fibroblast cells^[28] and possess bactericidal properties via oxidative stress,^[29] making it an excellent candidate for tissue engineering applications,^[30] bio-based materials for high performance scaffolds,^[31] or stimuli-responsive materials for drug delivery.^[32]

In this work, we present a series of nanocomposites manufactured via SL where GO is used both as a reinforcing agent and as a smart platform for material functionalization through simple surface modification reactions. On the one hand, the supramolecular interactions between GO and the photosensitive resin enhance the strength and toughness of the nanocomposites. On the other hand, the GO functional groups located on the surface of the material are available after printing the material, which allows their modification with different biomolecules (e.g., polysaccharides or proteins) that can act as biological cues. This combination, which gives the material improved mechanical and functional properties, shows the great potential of these nanocomposites in new, high demanding biomedical applications.

2. Results and Discussion

2.1. 3D Printing of the Nanocomposites and Evaluation of Their Mechanical Properties

Different amounts of GO nanoplates were dispersed in the resin by high shear mixing and degassed under vacuum to achieve a homogeneous distribution of GO and avoid the presence of air bubbles. Then, the resin precursor was poured into the tank and CAD files including structures with complex parts, monolayers and tensile testing specimens were loaded into the SL software. All the objects were successfully printed when GO concentrations up to 1.0 wt% were used, both at layer height of 100 and 200 μm . 1.0 and 2.5 wt% GO nanocomposites allowed the manufacturing of solid structures such as tensile testing specimens but failed in printing properly complex designs, resulting in irregular or partially printed objects with unfinished parts. For concentrations above 2.5 wt% GO, no objects could be printed. Additional tests where the dispersion time and speed of GO in the resin were increased did not cause any improvement in the printing of the nanocomposites. Likely, the GO nanoplates, able to partially absorb and scatter the laser light, hinder the proper photopolymerization of the resin.^[33] These results are in good agreement with our previous findings using graphene nanoplates of similar dimensions, where defective printing was also obtained for nanocomposites at concentrations above 2.5 wt%.^[34] **Figure 1** shows a lattice as an example of complex objects printed with 0.5 wt% GO (see also Figure S1a, Supporting Information). Scanning electron microscopy (SEM) images at low magnifications (Figure 1c,d) evidence that the layer height is in well agreement with the intended values (100 μm), indicating that, in this range of concentrations, the objects are accurately printed without sensible variations in their dimensions. More structures and at different concentrations and layer heights can be found in Figures

S2 and S3 (Supporting Information), illustrating the successful printing of sophisticated structures containing loops and hollow parts, at either 100 or 200 μm for different GO concentrations. Higher magnification SEM images (Figure 1e, Figure S4, Supporting Information) show that the GO is homogeneously distributed within the polymeric matrix as consequence of the well dispersion and compatibility between the filler and the matrix.

Mechanical properties of the nanocomposites were evaluated by tensile testing. For this purpose, ten tensile testing specimens were printed for each concentration (0, 0.1, 0.5, and 1.0 wt% GO), of which five specimens were post-cured inside a UV chamber at 60 °C for 60 min. In the case of 2.5 wt% GO nanocomposites, seven specimens were printed, of which three were post-cured. **Figure 2** and Figure S5 (Supporting Information) show the tensile behavior of the different nanocomposites as a function of the GO concentration. 0.1 and 0.5 wt% GO nanocomposites show an increase of the ductility right after printing (green samples, Figure 2a). Interestingly, the stress increases in the plastic region for 0.1 and 0.5 wt% GO nanocomposites after $\approx 15\%$ strain (when the pristine resin fails), suggesting that GO is able to participate in the fracture mechanism. This behavior can be explained attending to the polar groups present at the surface of GO, which may interact with the acrylic resin matrix via hydrogen bonding. These reversible, supramolecular interactions can be disassembled and reassembled under slow pulling, conferring the material with higher ductility, as it can be observed in the enhanced elongation at break of the nanocomposites, reaching twice the value of the pristine resin (Figure 2e) and in the increase of the tensile toughness in Figure 2f. The ductility of 0.1 wt% GO nanocomposites increases at expenses of a minimal loss in tensile strength and stiffness. However, in the case of 0.5 wt% GO nanocomposites, the stiffness and tensile strength also increases (Figure 2c,d), indicating that a significant number of GO nanoplates contribute to enhance the mechanical properties, playing a key role in the fracture mechanism. For GO contents above 1.0 wt%, all the mechanical properties decrease. This might be caused by a too high GO content which only allows partial polymerization of the resin, leading to a loose polymeric network with worsened mechanical properties. The trend follows towards lower values for 2.5 wt% GO nanocomposites. This can be correlated to the presence of GO partially blocking and scattering the laser, rendering less cured composites in comparison with pristine resin^[34] and it is probably the reason why the complex objects could not be properly printed when using these concentrations.

To enhance their mechanical properties, the nanocomposites underwent a typical post-curing process with UV light and temperature. This treatment promotes the crosslinking of the remaining free monomers within the material, creating new covalent bonds that increase the stiffness and strength of the material despite some loss of ductility. Such behavior can be observed for the pristine resin and all the GO nanocomposites in Figure 2b. After post-curing, tensile strength increases in a broad range from 20–30 to 60–75 MPa for resin contents up to 0.5 wt% GO. When these materials are compared after the post-curing, an increase in tensile strength is observed from 61.5 ± 1.9 MPa (pristine resin) to 63.9 ± 1.6 MPa (0.1 wt% GO) and 73.0 ± 2.9 MPa (0.5 wt% GO). This trend is in agreement with the behavior observed in the green samples, where it is assumed that the GO nanoplates play a key role in the structural

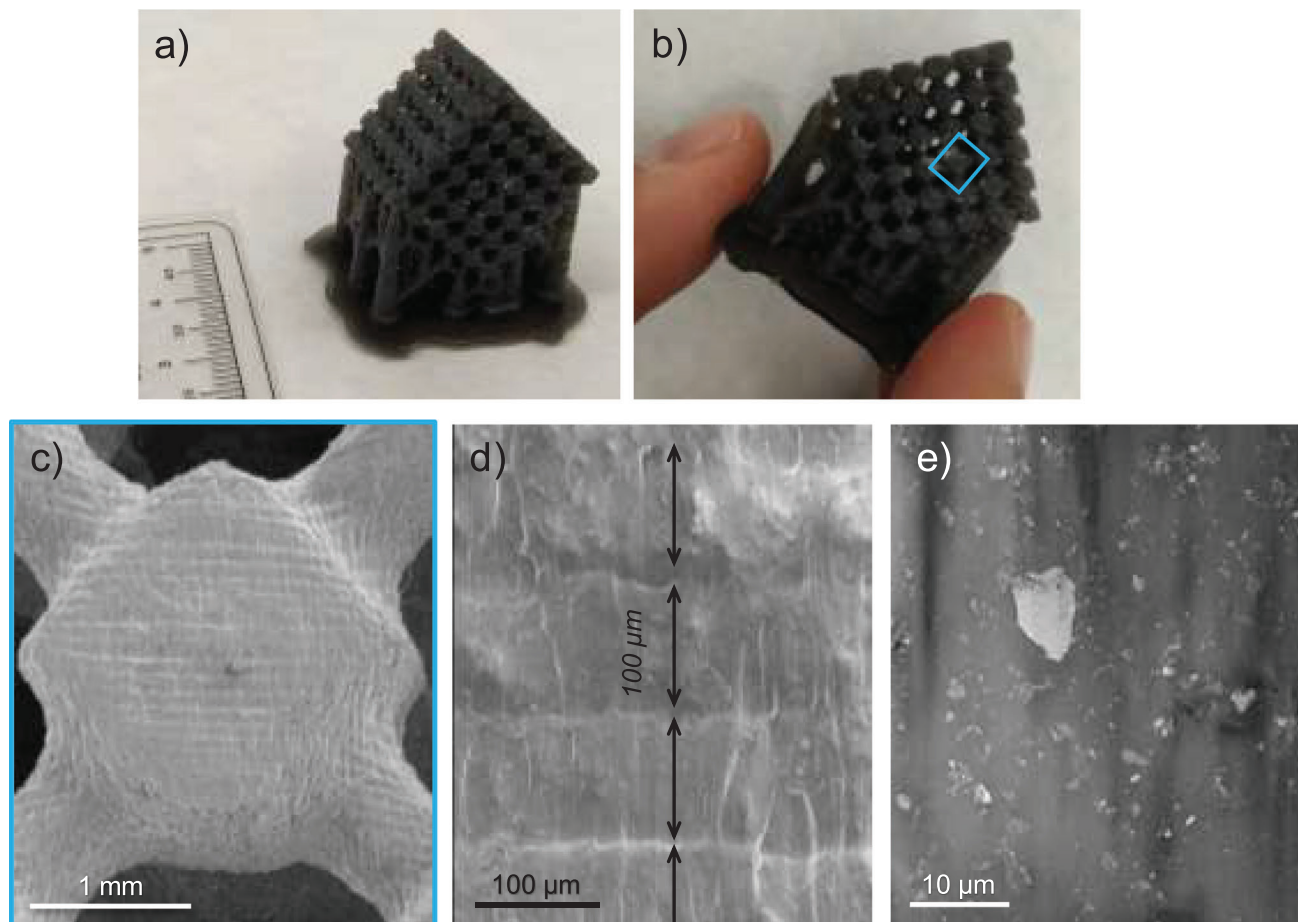


Figure 1. a,b) Digital photographs and c–e) SEM images of a cubic lattice (size $20 \times 20 \times 20$ mm) with complex geometry printed with resin containing 0.5 wt% GO using a layer height of $100 \mu\text{m}$. Blue square in (b) corresponds to the SEM image shown in (c); high-magnification SEM image in (e) shows a representative dispersion of the GO nanoplates with different sizes in the resin.

properties of the material. In all these cases, the elongation at break remains practically constant around 5%–7% strain, evidencing that there is no embrittlement of the material.

Other authors have observed similar trends for nanocomposites with similar GO concentrations, usually below 1.0 wt%. Lin et al.^[18] reported enhanced strength and ductility for printed nanocomposites containing 0.2 wt% GO, when compared to the pristine resin. In their case, they obtained stretchable materials with a strength of 14 MPa and an elongation at break around 22% after a post-processing combining UV light and temperature for 6 h. Manapat et al.^[23] observed worsened mechanical properties for green nanocomposites containing 0.1–1.0 wt% GO, obtaining soft nanocomposites with low strength right after printing. However, the nanocomposites exhibited a significant increase in the mechanical properties after thermal post-curing at $100 \text{ }^\circ\text{C}$, achieving tensile strength values of 50–60 MPa for 0.5–1.0 wt% GO nanocomposites without significant differences between these two concentrations. Palaganas et al.^[24] reported enhanced strength and toughness for 0.2 wt% GO nanocomposites after GO polymerization with methyl acrylate. Nanocomposites containing 1.0 wt% unmodified GO presented higher strength and elongation values than their functionalized coun-

terpart, indicating that GO alone already has a good compatibility with SL methacrylic resins. Guo et al.^[26] were able to reach concentrations up to 5 wt% after GO surface modification with an amine-containing dispersant. These films were highly flexible and thermally stable although lower hardness values were observed when compared to the pristine resin. In our study, an increase in strength and toughness was found when using 0.1–0.5 wt% GO concentrations before and after post-processing. As this GO was not previously modified, the GO itself has enough compatibility with SL acrylic resins to be well dispersed and homogeneously distributed, as it is shown in Figure 1e and Figure S4 (Supporting Information). Moreover, we hypothesize that the high O content (41 at%), in the forms of epoxy, hydroxyl, and carboxylic acid forms, enhances the compatibility with the resin via hydrogen bonding.^[23] This also is in agreement with other previous works, where non-polar GNPs were used and the ductility of the nanocomposite was not enhanced in any case due to the absence of supramolecular forces between the matrix and the filler.^[34–36]

Given the interesting mechanical properties of these materials, in particular of 0.5 wt% GO nanocomposites, the fracture and lateral surfaces of the dogbone specimens were examined in

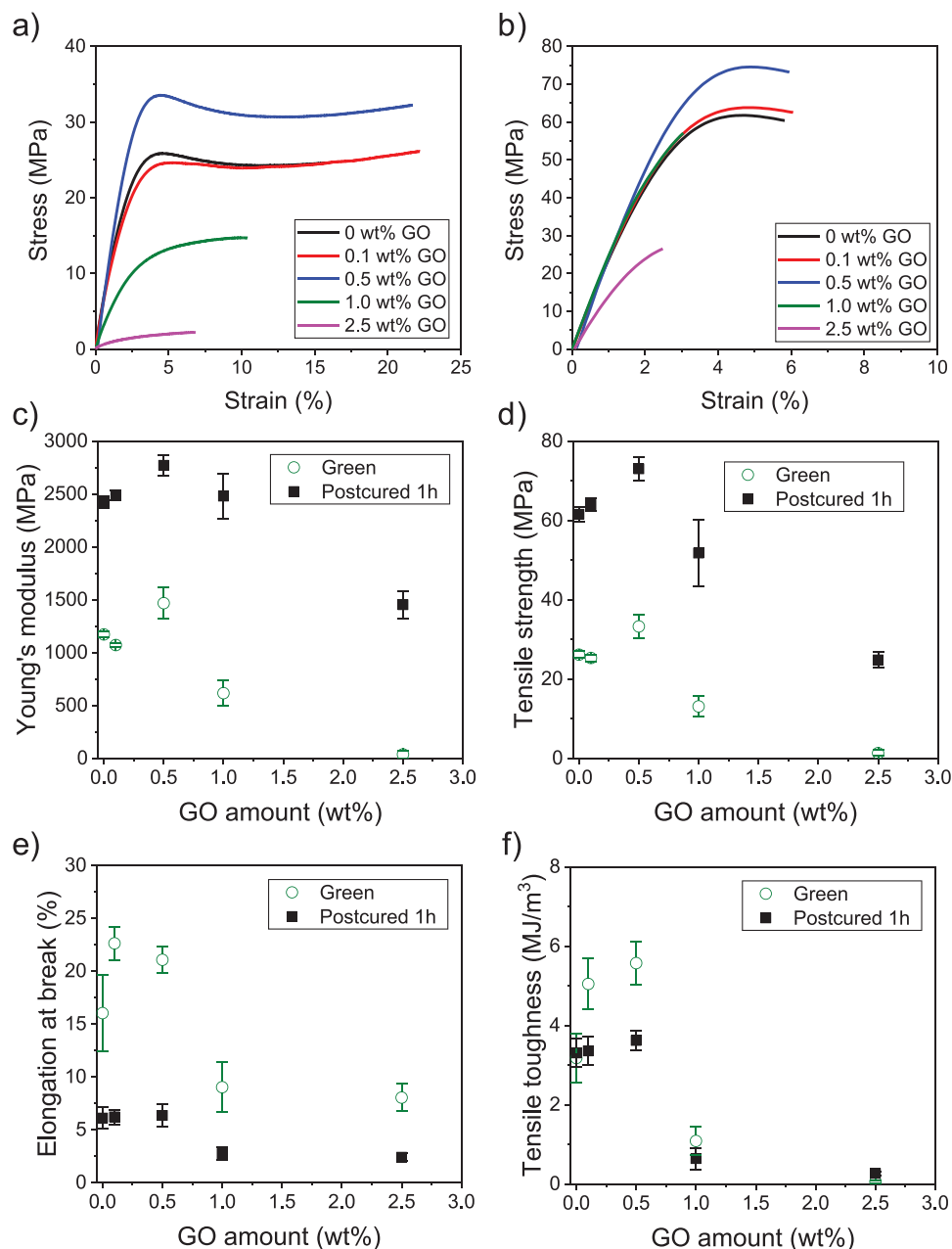


Figure 2. Representative tensile testing curves of nanocomposites containing 0–2.5 wt% GO a) after printing (green samples) and b) after post-curing with UV for 60 min (post-cured samples); average c) Young's modulus, d) tensile strength, e) elongation at break, and f) tensile toughness of the nanocomposites.

more detail after testing. **Figure 3a,b** shows the fracture surface of the resin without any GO. The shape of the surface is quite uneven, evidencing a certain ductile behavior of the material, as it was previously discussed in Figure 2. A similar morphology is observed in Figure 3c,d, while the analyses also reveal the presence of GO nanoplates in the fracture (see Figure 3e) area well-embedded within the resin deformed in the same manner than the polymeric matrix. The placement of nanoplates at the breaking surface is indicative of their participation in the fracture mechanism, evidencing the increase in the mechanical properties of 0.5 wt% nanocomposites. Moreover, the mate-

rial toughening may lead to plastic deformation at the fracture surfaces,^[37] also related to longer crack propagation before break. In a similar manner, GO nanoplates can be observed at the lateral sides of the tensile testing specimens (Figure 3f–h and Figure S4, Supporting Information), bending following the surface roughness and well-adapted to the polymeric matrix, supporting the hypothesis of the good compatibility between GO and the resin.

Transmission electron microscopy (TEM) analyses further allowed the identification and location of the GO additive within the polymer matrix. Electron-transparent samples of the composite were obtained from the core of the tensile specimen

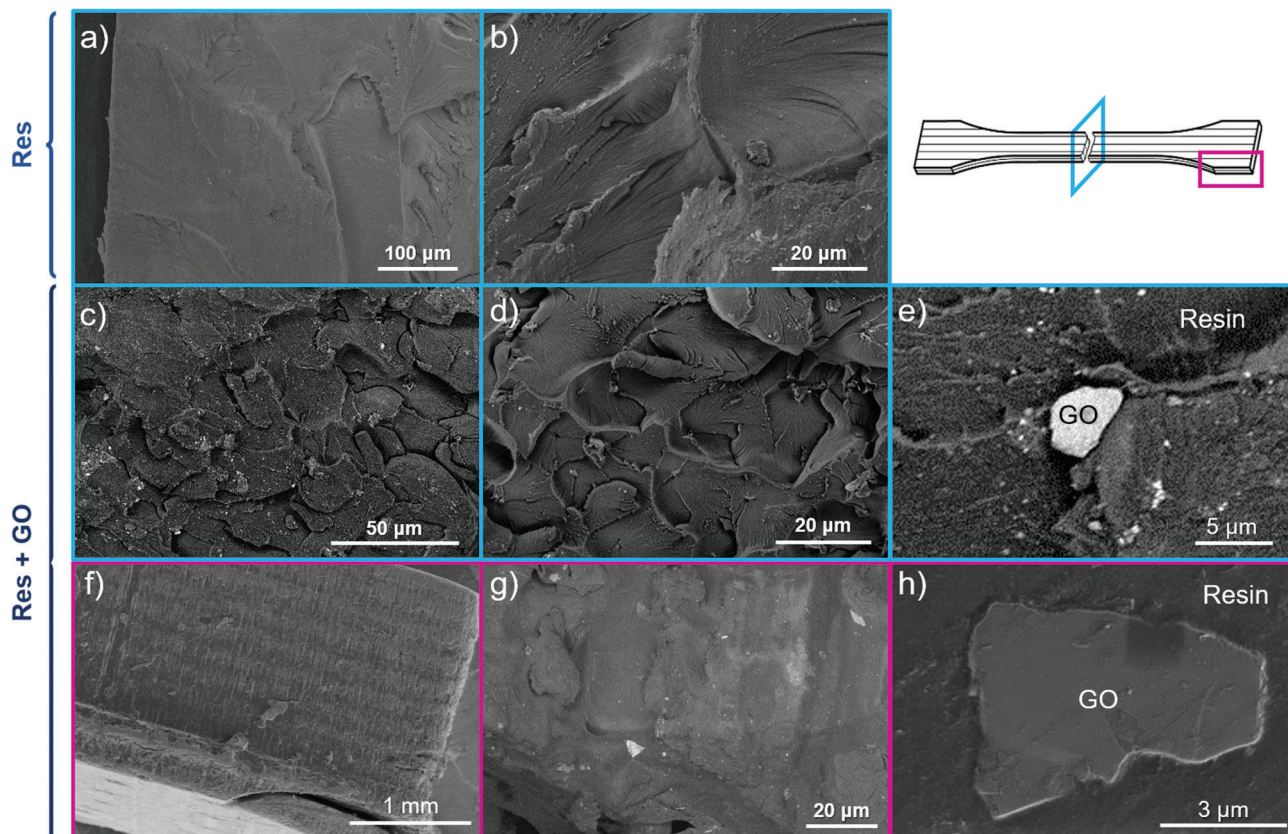


Figure 3. Fracture and lateral surfaces after tensile testing of printed dogbone specimens with a–e) pristine resin and c–h) resin containing 0.5 wt% GO. SEM images framed in cyan (a–e) correspond to the fracture surface while images framed in magenta (f–h) correspond to a lateral surface as indicated in the drawing in the upper right corner.

after the test (see **Figure 4a**). Interestingly, most of the observed GO nanoplates are assembled into bunches, containing few wrinkled and/or folded nanoplates, distributed within the resin (**Figure 4a**). The presence and morphology of such aggregates is addressed by high-angle annular dark field (HAADF), providing Z-contrast images (**Figure 4b,c**) and TEM measurements, including high-resolution imaging, HRTEM, of the GO (**Figure 4d–f**). GO nanoplates render atomic resolution images of the crystalline structure, with dominance of (001) planes (note the bending of the atomic planes in **Figure 4f**), following the curvature of the nanoplates observed at lower magnifications, i.e., in **Figure 4e**. Energy-dispersive X-ray (EDX) analysis performed evidence the richer O content of the GO nanoplates (up to 50 at% O, according to the manufacturer) compared to the acrylic resin (**Figure 4g**). Even though some traces of non-exfoliated GO can be observed (see **Figure S4f,g**, Supporting Information), SEM and TEM results show a homogenous distribution of few-layer thick GO nanoplates within the polymeric resin. A higher exfoliation of GO, increasing the time or speed of the dispersion, can lead to an even better distribution of GO, which may further improve the mechanical properties of the nanocomposites. X-ray diffraction (XRD) and Raman spectroscopy complementary analysis were performed for a better understanding of the composition and morphology of the GO, and determine the possible formation of reduced graphene oxide (rGO) after printing and post-curing

(see **Figures S6 and S7**, Supporting Information). The characteristic (001) and (002) peaks of graphene-derived materials are not observed in XRD, neither before nor after post-curing. This may indicate that the GO is well dispersed and with a good de-agglomeration degree, or that the amount of GO is too low to be detected by XRD, covered by the broad signal from the highly amorphous polymer matrix. Raman analysis show that the I_D/I_G ratio of GO in the composites is 1.0, suggesting the absence of rGO (with typical I_D/I_G ratios below 0.90) during either the printing or post-curing process.^[38,39] This is supported by the EDX results, which show O at% amounts characteristic of GO, even though some formation of rGO with high content of O is also possible. In any case, the morphology observed in **Figure 4** implies a high interface of GO with the resin. Their wrinkled and folded disposition suggests that the increase in the strength and ductility of the nanocomposites is promoted by the unfolding and stretching of GO when an external force is applied.

2.2. Nanocomposites as Functional Platforms: Immobilization of Biomolecules in Surface

After studying the structural behavior of the GO nanocomposites, their applicability as platforms for biomolecule immobilization is assessed. For this purpose, monolayers of 0.5 wt% GO

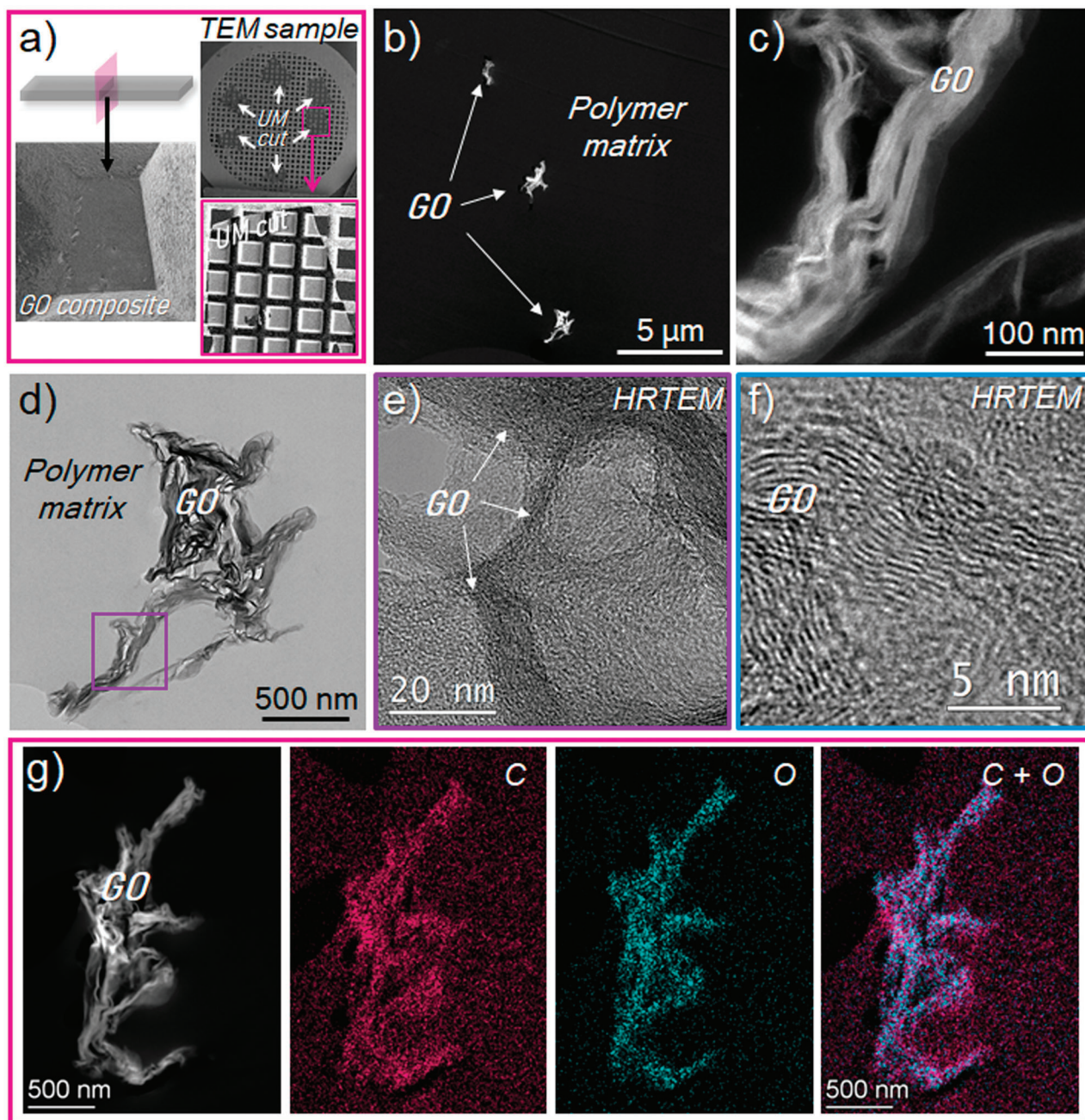


Figure 4. TEM analysis of the 0.5 wt% GO nanocomposite. Electron-transparent sample prepared from the core of the tensile specimen as shown in (a); b,c) HAADF measurements; d–f) TEM and HRTEM measurements and g) carbon (magenta) and oxygen (cyan) EDX maps acquired at the region shown in the left image. Right panel displays C and O maps together.

nanocomposites were printed and surface modification of GO was performed via 1-ethyl-3-(3-dimethyl aminopropyl) carbodiimide (EDC) coupling. **Figure 5** shows a scheme of the surface modification of GO nanoplates with chitosan (CHI) via a simple amidation coupling chemistry working in mild conditions. Functionalization of GO in surface was performed under acidic conditions to enhance the solubility of CHI. This also favors the reaction with N-hydroxysuccinimide (NHS) and EDC of the carboxylic acid and epoxy groups present at the surface of GO with

the primary amines of CHI.^[40] GO surface modification is carried out via covalent bonds, so CHI will remain at the surface after any washing step including surfactants or other detergents typically used in biological assays.

CHI is a biopolymer which is naturally present in the extracellular matrix of living organisms and possesses biological function in protein recognition processes, such as bovine serum albumin (BSA). Thus, the immobilization of CHI at the surface of the GO nanoplates was checked by the subsequent interaction

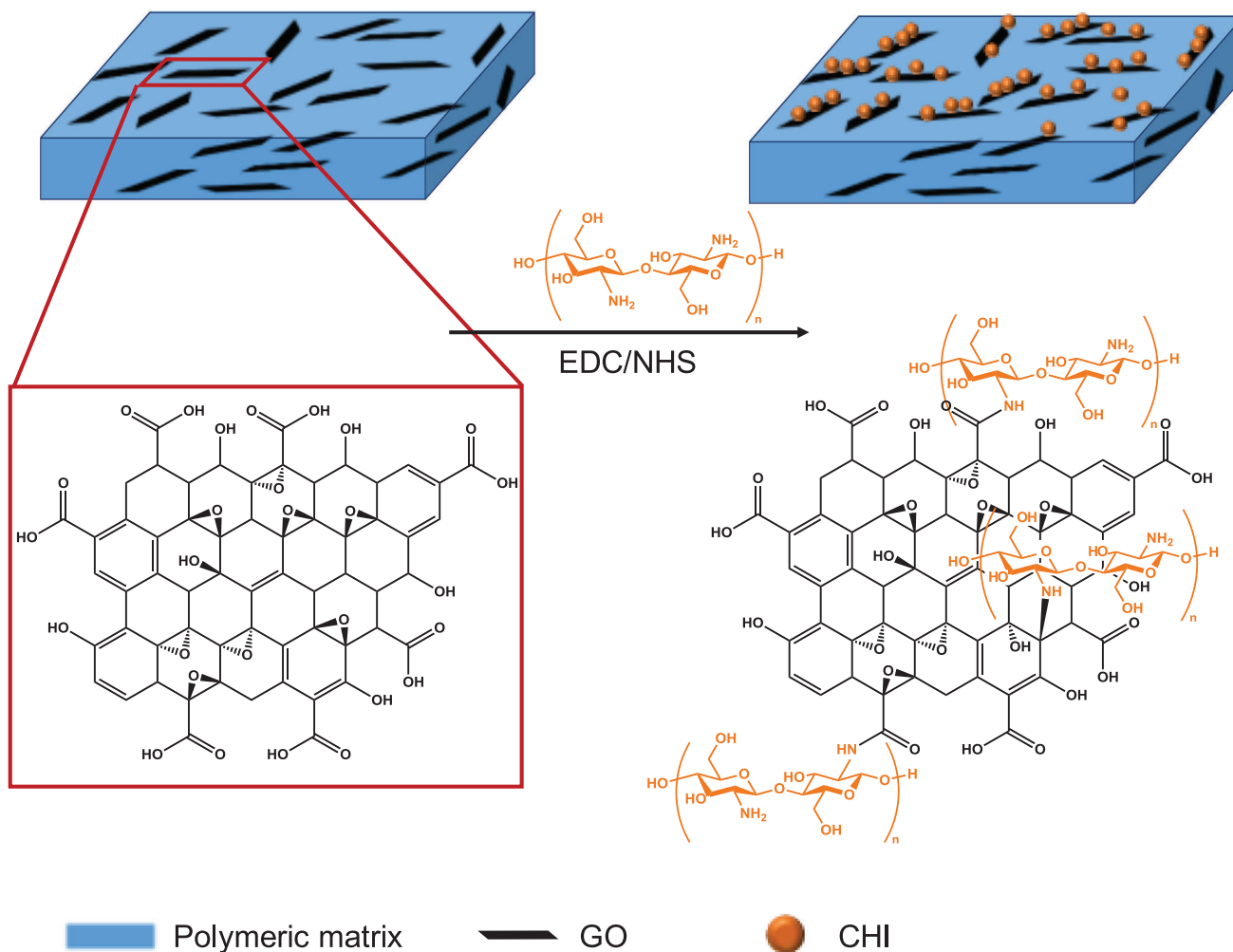


Figure 5. Scheme depicting the surface modification of GO with CHI via EDC coupling.

with a fluorescently labeled BSA. This protein is well-known to interact with CHI via specific interactions ligand–protein,^[41] and it is widely used in diagnostic tools for early detection of diseases.^[42] Figure 6 and Figure S8 (Supporting Information) show regularly distributed patterns corresponding to immobilized BSA indicating the successful attachment of CHI onto the GO surface. A closer look (Figure 6c) demonstrates that the sizes of the fluorescence features are comparable to that of the GO nanoplates. A negative control was also done incubating a printed surface containing no GO with CHI in the same conditions as the 0.5 wt% GO nanocomposites. It was observed that, under the same exposure conditions, there is no fluorescence (Figure S9, Supporting Information).

Alkaline phosphatase (ALP) enzyme was also immobilized onto the GO surfaces to prove the versatility of the nanocomposites as functional platforms. ALP is widely used as a biomarker in bone repair research to evaluate the osteoblasts activity.^[43,44] The reaction proceeds in similar conditions as in the case of CHI immobilization but at pH 6–7 to ensure ALP is above its isoelectric point ($pI = 4.4\text{--}5.8$, according to the supplier). In this case, it is expected that the free amines present in the lysine residues of

ALP can react with the carboxylic acid and epoxy groups of GO at the surface. These amines are known to stabilize the ALP in aqueous media so that they are accessible for reaction with GO. It should be noted that the scheme presented in Figure 7a is not made to scale. ALP has a size of 2–4 nm while GO possess lateral sizes of several microns, rendering high protein loads per GO nanoplate.

The successful immobilization of ALP was monitored by studying the dephosphorylation of *p*-nitrophenylphosphate (pNPP). This reaction produces *p*-nitrophenol (pNP), a yellow-colored product that can be easily monitored by UV–vis spectroscopy. The rate of pNP formation allows determining the catalytic activity of the ALP adsorbed on the GO nanoplates. Similar to what was done with the CHI–BSA interaction, we also performed a test control in a surface without GO after immobilizing the ALP. Figure 7b and Figure S10 (Supporting Information) show the dephosphorylation of pNPP into pNP. It can be observed a significant increase in the formation of pNP when ALP is immobilized onto the nanocomposites containing GO. This indicates not only that ALP is successfully immobilized, but that also its biological function remains active after

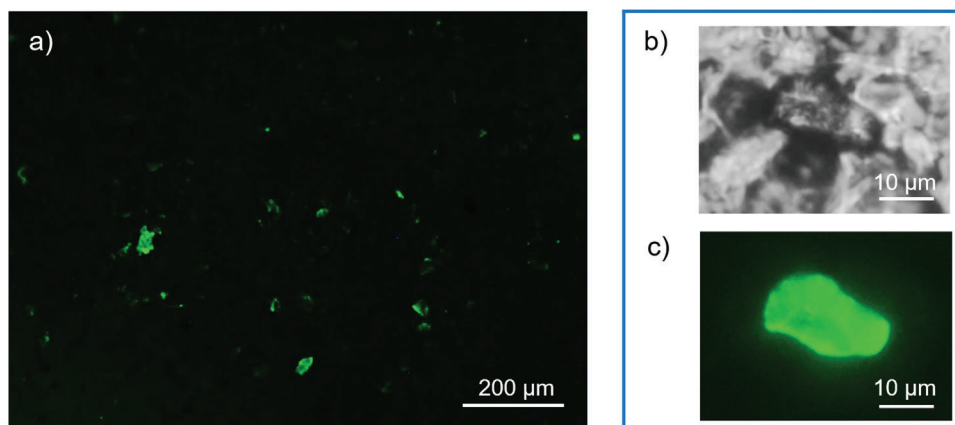


Figure 6. BSA-FITC immobilized at the surface of a 0.5 wt% GO nanocomposite previously functionalized with CHI; a) fluorescent image showing a general view of the surface (10 \times); b) bright field optical image and c) fluorescent image of a GO nanoplate (40 \times).

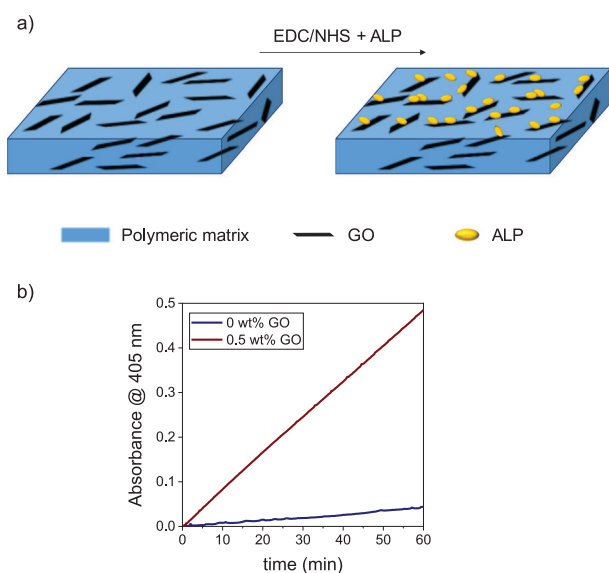


Figure 7. a) Scheme of surface functionalization of GO with ALP; b) absorbance of pNP measured at 405 nm at different times for surfaces containing 0 and 0.5 wt% GO.

Table 1. Catalytic activity of the dephosphorylation of pNPP for surfaces containing 0 and 0.5 wt% GO after functionalization with ALP.

	Catalytic activity [mM min^{-1}]
0 wt% GO	0.039 ± 0.002
0.5 wt% GO	0.444 ± 0.005

the chemical reaction and subsequent washing. In the case of surfaces without GO there is a small catalytic activity, probably due to non-specific adsorption of ALP onto the polymer surface caused by the high excess used in the GO functionalization step, as it was observed previously on other polymeric surfaces.^[45] However, the catalytic activity data presented in **Table 1** shows meaningful differences between the 0.5 wt% GO nanocomposites and the pristine resin, with a tenfold increased speed

in the formation of pNP, evidencing the successful selective immobilization of ALP on the GO surfaces.

3. Conclusions

We have developed a series of functional nanocomposites via SL with enhanced mechanical properties due to good interaction between the GO and the acrylic resin via noncovalent interactions. In particular, 0.5 wt% GO nanocomposites exhibited increased strength, stiffness, and ductility when compared to the pristine resin. Moreover, these nanocomposites are also suitable as platforms for selective immobilization of CHI and ALP using facile coupling strategies. After surface functionalization of GO, the biomolecules remained active, being able to perform recognition processes such as protein–ligand interaction or enzymatic catalysis. This evidences the versatility of these nanocomposites, allowing their use for different biomedical applications such as biosensing or tissue engineering which require durable and functional materials on demand.

4. Experimental Section

Materials: GO nanoplates (41–50 at% O, lateral size < 28 μm) were purchased from Graphenea. Form Clear resin v2 (photoinitiator and mixture of acrylic monomers and oligomers) was purchased from Formlabs. EDC, NHS, CHI ($M_w = 100\text{--}300 \text{ kg mol}^{-1}$), pNPP disodium salt hexahydrate, sodium chloride (NaCl), and tris(hydroxymethyl)methylamine (Tris) were purchased from Acros organics. ALP from bovine intestinal mucosa and fluorescein-isothiocyanate labeled bovine serum albumin (BSA-FITC) were purchased from Sigma. Hydrochloric acid (HCl), acetic acid (HAc), and isopropyl alcohol (iPA) were purchased from Scharlab. All reagents were used as received.

Fabrication of Nanocomposites via Stereolithography: Nanocomposite precursors containing the photosensitive resin with different GO contents (0.1–2.5 wt%) were prepared by high shear mixing using a Eurostar 20 (IKA) at 2000 rpm at room temperature for at least 15 min. The obtained dispersion was then degassed under vacuum. The precursors were then poured onto a tank and samples were 3D-printed in a stereolithography printer Form 1+ (Formlabs) using a 405 nm laser with an output power of 120 mW and a spot size of 140 μm . Layer height was varied between 100 and 200 μm and different objects including monolayers, complex structures, and 1BA dogbone specimens according to ISO 527-2 were

printed. Figure S1 (Supporting Information) shows the CAD files of the complex structures (i.e., hollow cubes and butterflies). Printed objects were then detached from the printer platform and washed with iPA for at least 15 min. Post-processing of the samples was performed for 60 min in a UV-chamber (FormCure, Formlabs) previously heated at 60 °C with a light source of 405 nm and power of 1.25 mW cm⁻².

Material Characterization: Tensile testing of dogbone specimens was performed in a universal testing machine (Shimadzu) at a constant speed of 1 mm min⁻¹ according to ISO 527-2. At least five specimens for materials containing 0–1.0 wt% GO and three specimens for 2.5 wt% GO nanocomposites were tested. Young's modulus, tensile strength, elongation at break, and tensile toughness values were dissected for each one of the measured specimens. Young's modulus was determined as the slope between 0.05% and 0.5% strain in the stress–strain plots. Tensile strength was obtained as the maximum stress value in the curve. Elongation at break was obtained as the strain value at the rupture point (maximum value in the X-axis). Tensile toughness was calculated as the area under the stress–strain curve. Results were averaged and standard deviations were presented as error bars. XRD of the composites was measured using a Bruker D8 ADVANCE using a Cu K α radiation source operated at a voltage of 40 kV with a scanning range of 5°–80°. Raman spectroscopy experiments were performed in a JASCO NRS-5100 spectrometer coupled to an optical microscope using a green laser ($\lambda = 532$ nm) with an output power of 0.4 mW. The Raman scattered light was detected on a thermoelectrically cooled CCD detector with an integration time of 10 s.

Electron Microscopy Measurements: SEM analyses were carried out in a FEI Nova NanoSEM 450 microscope equipped with a field-emission gun. Composite materials were directly measured, avoiding any sample preparation before observation. TEM studies were performed by using a Thermo Scientific Talos operated at 200 kV achieving TEM line resolution below 0.1 nm, and equipped with a ChemiSTEM EDX detector. EDX analyses were performed under scanning mode (STEM). Electron transparent sections of the materials were prepared by ultramicrotomy using a diamond knife and directly deposited onto TEM grids.

Surface Modification of GO with Biomolecules: Monolayers of 0.5 wt% GO nanocomposites (0.2 mm \times 5 mm \times 5 mm) were immersed in a buffer solution (0.150 M NaCl, 0.015 M HAC, pH 3–4) containing EDC (1 mg mL⁻¹), NHS (5 mg mL⁻¹), and CHI (1 mg mL⁻¹) for 3 h under shaking at 300 rpm. After reaction, surfaces were thoroughly washed with the same buffer. Then, surfaces were immersed in a BSA-FTIC (0.5 mg mL⁻¹) aqueous solution for 30 min and subsequently washed before examination under an Olympus IX83 inverted microscope equipped with a set of filters for FITC. An alternative surface modification was also carried out using ALP instead of CHI. In this case, the immobilization of ALP was evidenced by monitoring the formation of pNP at different times ($\epsilon_{405\text{ nm}} = 18\,500\text{ M}^{-1}\text{ cm}^{-1}$) in a UV–vis Varian Cary 50 Conc spectrophotometer. For this purpose, an excess of pNPP (5.6 \times 10⁻³ M) in 0.150 M NaCl and 0.01 M Tris buffer (pH 8) was used. The catalytic activity was calculated as the slope of the pNP concentration versus time, after applying the Lambert–Beer equation ($A = b \cdot \epsilon \cdot c$; $b = 1$ cm) to the absorbance values recorded every 10 s at a wavelength of 405 nm for 1 h. Surface modification of the resin without GO was also performed as negative control.

Supporting Information

Supporting Information is available from the Wiley Online Library or from the author.

Acknowledgements

This work was funded by the Ministry of Science, Innovation and Universities (TEC2017-86102-C2-2-R), the 2014-2020 ERDF Operational Programme and the Department of Economy, Knowledge, Business and University of the Regional Government of Andalusia (FEDER-UCA18-106586). Co-funding from UE and the research group INNANOMAT (ref. TEP-946) is also acknowledged. A.S.d.L. and M.d.I.M. acknowledge Ministry of Science, Innovation and Universities for their Juan de la Cierva Incorporación

postdoctoral fellowships (IJC2019-041128-I, IJCI-2017-31507). SEM and TEM measurements were carried out at the DME-SC-ICyT-ELECOMI-UCA.

The copyright line for this article was changed on 27 May 2022 after original online publication.

Conflict of Interest

The authors declare no conflict of interest.

Data Availability Statement

The data that support the findings of this study are available from the corresponding author upon reasonable request.

Keywords

functional materials, graphene oxide, nanocomposites, stereolithography, surface modification

Received: October 19, 2021

Revised: December 23, 2021

Published online: January 24, 2022

- [1] L.-D. Koh, J. Yeo, Y. Y. Lee, Q. Ong, M. Han, B. C.-K. Tee, (*Invited review*), *Mater. Sci. Eng., C* **2018**, *86*, 151.
- [2] G. Maduraiveeran, M. Sasidharan, V. Ganesan, *Biosens. Bioelectron.* **2018**, *103*, 113.
- [3] B. Zhang, X. Pei, P. Song, H. Sun, H. Li, Y. Fan, Q. Jiang, C. Zhou, X. Zhang, *Composites, Part B* **2018**, *155*, 112.
- [4] G. Turnbull, J. Clarke, F. Picard, P. Riches, L. Jia, F. Han, B. Li, W. Shu, *Bioact. Mater.* **2018**, *3*, 278.
- [5] K. M. Ferlin, M. E. Prendergast, M. L. Miller, D. S. Kaplan, J. P. Fisher, *Acta Biomater.* **2016**, *32*, 161.
- [6] T. D. Ngo, A. Kashani, G. Imbalzano, K. T. Q. Nguyen, D. Hui, *Composites, Part B* **2018**, *143*, 172.
- [7] J. Dos Santos, R. S. Oliveira, T. V. Oliveira, M. C. Velho, M. V. Konrad, G. S. Da Silva, M. Deon, R. C. R. Beck, *Adv. Funct. Mater.* **2021**, *31*, 2009691.
- [8] K. Charbonnier, M. Hadida, D. Marchat, *Acta Biomater.* **2021**, *121*, 1.
- [9] J. Huang, H. O. T. Ware, R. Hai, G. Shao, C. Sun, *Adv. Mater.* **2021**, *33*, 2005672.
- [10] V. Hahn, P. Kiefer, T. Frenzel, J. Qu, E. Blasco, C. Barner-Kowollik, M. Wegener, *Adv. Funct. Mater.* **2020**, *30*, 1907795.
- [11] C. Garot, G. Bettega, C. Picart, *Adv. Funct. Mater.* **2021**, *31*, 2006967.
- [12] A. Goyanes, U. Det-Amornrat, J. Wang, A. W. Basit, S. Gaisford, *J. Controlled Release* **2016**, *234*, 41.
- [13] V. B. Morris, S. Nimbalkar, M. Younesi, P. McClellan, O. Akkus, *Ann. Biomed. Eng.* **2017**, *45*, 286.
- [14] Z. Weng, Y. Zhou, W. Lin, T. Senthil, L. Wu, *Composites, Part A* **2016**, *88*, 234.
- [15] H. Gong, M. Beauchamp, S. Perry, A. T. Woolley, G. P. Nordin, *RSC Adv.* **2015**, *5*, 106621.
- [16] S. K. Ghorai, S. Maji, B. Subramanian, T. K. Maiti, S. Chattopadhyay, *Carbon* **2019**, *141*, 370.
- [17] D. Ponnamma, Y. Yin, N. Salim, J. Parameswaranpillai, S. Thomas, N. Hameed, *Composites, Part B* **2021**, *204*, 108493.
- [18] D. Lin, S. Jin, F. Zhang, C. Wang, Y. Wang, C. Zhou, G. J. Cheng, *Nanotechnology* **2015**, *26*, 434003.
- [19] J. Z. Manapat, Q. Chen, P. Ye, R. C. Advincula, *Macromol. Mater. Eng.* **2017**, *302*, 1600553.

- [20] J. Li, L. Wang, L. Dai, L. Zhong, B. Liu, J. Ren, Y. Xu, *J. Mater. Sci.* **2018**, 53, 1874.
- [21] Y. Li, Z. Feng, L. Huang, K. Essa, E. Bilotti, H. Zhang, T. Peijs, L. Hao, *Composites, Part A* **2019**, 124, 105483.
- [22] H. Korhonen, L. H. Sinh, N. D. Luong, P. Lehtinen, T. Verho, J. Partanen, J. Seppälä, *Phys. Status Solidi A* **2016**, 213, 982.
- [23] J. Z. Manapat, J. D. Mangadlao, B. D. B. Tiu, G. C. Tritchler, R. C. Advincula, *ACS Appl. Mater. Interfaces* **2017**, 9, 10085.
- [24] J. O. Palaganas, N. B. Palaganas, L. J. I. Ramos, C. P. C. David, *ACS Appl. Mater. Interfaces* **2019**, 11, 46034.
- [25] Y. Yuan, Z. Liu, B. Wei, Z. Yang, L. Wang, W. Fei, *Dalton Trans.* **2020**, 49, 1752.
- [26] B. Guo, X. Ji, W. Wang, X. Chen, P. Wang, L. Wang, J. Bai, *Composites, Part B* **2021**, 208, 108598.
- [27] P. Li, L. Zhao, Z. Jiang, M. Yu, Z. Li, X. Li, *Macromol. Mater. Eng.* **2019**, 304, 1900504.
- [28] Q. Chen, J. D. Mangadlao, J. Wallat, A. De Leon, J. K. Pokorski, R. C. Advincula, *ACS Appl. Mater. Interfaces* **2017**, 9, 4015.
- [29] F. Perreault, A. F. De Faria, S. Nejati, M. Elimelech, *ACS Nano* **2015**, 9, 7226.
- [30] F. Rostami, E. Tamjid, M. Behmanesh, *Mater. Sci. Eng., C* **2020**, 115, 111102.
- [31] H. Baniasadi, S. Borandeh, J. Seppälä, *Macromol. Mater. Eng.* **2021**, 306, 2100255.
- [32] L. Zhang, X. Zhang, L. Li, Y. Liu, D. Wang, L. Xu, J. Bao, A. Zhang, *Macromol. Mater. Eng.* **2020**, 305, 1900718.
- [33] G. Gonzalez, A. Chiappone, I. Roppolo, E. Fantino, V. Bertana, F. Perucci, L. Scaltrito, F. Pirri, M. Sangermano, *Polymer* **2017**, 109, 246.
- [34] A. S. De León, S. I. Molina, *Polymers* **2020**, 12, 1103.
- [35] Y. Zhang, Y. Wang, J. Yu, L. Chen, J. Zhu, Z. Hu, *Polymer* **2014**, 55, 4990.
- [36] R. J. Young, M. Liu, I. A. Kinloch, S. Li, X. Zhao, C. Vallés, D. G. Papa-georgiou, *Compos. Sci. Technol.* **2018**, 154, 110.
- [37] *Failure Analysis and Fractography of Polymer Composites* (Ed: E. S. Greenhalg), Woodhead Publishing, **2009**, pp. 164–237.
- [38] S. Muhammad Hafiz, R. Ritikos, T. J. Whitcher, N. Md. Razib, D. C. S. Bien, N. Chanlek, H. Nakajima, T. Saisopa, P. Songsiriritthigul, N. M. Huang, S. A. Rahman, *Sens. Actuators, B* **2014**, 193, 692.
- [39] S. Perumbilavil, P. Sankar, T. P. Rose, R. Philip, *Appl. Phys. Lett.* **2015**, 107, 051104.
- [40] T. Liu, W. Dan, N. Dan, X. Liu, X. Liu, X. Peng, *Mater. Sci. Eng., C* **2017**, 77, 202.
- [41] L. Bekale, D. Agudelo, H. A. Tajmir-Riahi, *Colloids Surf., B* **2015**, 125, 309.
- [42] M. D. T. Torres, W. R. De Araujo, L. F. De Lima, A. L. Ferreira, C. De La Fuente-Nunez, *Matter* **2021**, 4, 2403.
- [43] A. Sabokbar, P. J. Millett, B. Myer, N. Rushton, *Bone Miner.* **1994**, 27, 57.
- [44] K.-F. Lin, S. He, Y. Song, C.-M. Wang, Y. Gao, J.-Q. Li, P. Tang, Z. Wang, L. Bi, G.-X. Pei, *ACS Appl. Mater. Interfaces* **2016**, 8, 6905.
- [45] A. S. León, R. M. Frutos, S. I. Molina, *Macromol. Mater. Eng.* **2020**, 305, 2000461.